Geochemistry, Geophysics, Geosystems

RESEARCH ARTICLE
10.1029/2020GC008950

Serpentinization, Deformation, and Seismic Anisotropy in the Subduction Mantle Wedge

Charis Horn[1], **Pierre Bouilhol**[2], **and Philip Skemer**[1]

[1]Department of Earth and Planetary Sciences, Washington University in St. Louis, St. Louis, MO, USA, [2]CRPG, Université de Lorraine-CNRS, UMR 7358, 15 Rue Notre Dame des Pauvres, Vandoeuvre-les-Nancy, France

Key Points:
- Deformed antigorite could account for some of the observed shear wave splitting at subduction zones
- Antigorite can also form nonrandom fabrics by replacing olivine in a topotactic manner
- However, antigorite which grew in a topotactic manner is only weakly anisotropic and is unlikely to contribute to shear wave splitting

Correspondence to:
C. Horn,
cmhorn@wustl.edu

Citation:
Horn, C., Bouilhol, P., & Skemer, P. (2020). Serpentinization, deformation, and seismic anisotropy in the subduction mantle wedge. *Geochemistry, Geophysics, Geosystems*, *21*, e2020GC008950. https://doi.org/10.1029/2020GC008950

Received 28 JAN 2020
Accepted 15 MAR 2020

Abstract Antigorite is a hydrous sheet silicate with strongly anisotropic seismic and rheological properties. Hydrous minerals such as antigorite have been invoked to explain numerous geologic observations within subduction zones including intermediate-depth earthquakes, arc volcanism, the persistent weakness of the subduction interface, trench-parallel *S* wave splitting, and episodic tremor and slip. To understand how the presence of antigorite-bearing rocks affects observations of seismic anisotropy, three mylonites from the Kohistan palaeo-island arc in Pakistan were analysed using electron backscatter diffraction. A fourth sample, which displayed optical evidence for crystallographically controlled replacements of olivine, was also investigated using electron backscatter diffraction to identify potential topotactic relationships. The resulting data were used to model the bulk seismic properties of antigorite-rich rocks. The mylonitic samples exhibit incredibly strong bulk anisotropy (10–20% for the antigorite + olivine). Within the nominally undeformed protomylonite, two topotactic relationships were observed: (1) (010)ant//(100)ol with [100]ant//[001]ol and (2) (010)ant//(100)ol with [100]ant//[010]ol. However, the strength of a texture formed by topotactic replacement is markedly weaker than the strength of the textures observed in mylonitic samples. Since antigorite is thought to be rheologically weak, we hypothesise that microstructures formed from topotactic reactions will be progressively overprinted as deformation is localised in regions with greater percentages of serpentine. Regions of highly sheared serpentine, therefore, have the potential to strongly influence seismic wave speeds in subduction settings. The presence of deformed antigorite in a dipping structure is one explanation for observations of both the magnitude and splitting pattern of seismic waves in subduction zones.

Plain Language Summary Subduction zones are regions on the Earth's surface where one tectonic plate sinks beneath another, generating large-magnitude earthquakes and explosive volcanism. Serpentine group minerals, due to their unusual material properties, are thought to play an important role in the subduction system. Antigorite, a type of serpentine, has vastly different properties depending on the orientation of the crystal. For example, the velocity at which a seismic wave can travel varies by as much as 66% between the fastest and slowest orientations of a single antigorite crystal. However, crystals of antigorite can become aligned by deformation or by replacing other crystals that had themselves previously been aligned, which complicates the interpretation of seismological data. This study analysed the orientations of antigorite crystals in exposed mantle rocks from Pakistan in order to understand the difference between the deformed and the substituted antigorite. We find that the pattern of seismic wave speeds at subduction zones is difficult to replicate by antigorite that overgrew earlier crystals but that deformed antigorite could explain some of the complexity observed in the distribution of seismic wave speeds at many subduction zones.

1. Introduction

Subduction zones are regions of complex deformation, with numerous interactions between metamorphic reactions and the rheologies of the phases in the system. One mineral group that has risen to prominence as a potential candidate to explain diverse observations of subduction zones is serpentine, a class of hydrous layer silicates that form as water interacts with mantle rocks (e.g., Mével, 2003). Mid-ocean ridge hydrothermal processes result in the formation of serpentine and other hydrous phases within the shallow slab mantle (Bonatti et al., 1974; Guillot et al., 2015; Juteau et al., 1990; Viti & Mellini, 1998), and subsequent brittle deformation allows for localised infiltration of water to depths of up to tens of kilometers (Cai et al., 2018; Cannat et al., 1992; Francis, 1981; Lefeldt et al., 2012; Ranero et al., 2003; White et al., 1984). This

structurally bound water is then carried along by the motion of the oceanic plates toward subduction zones. Geological observations (Fryer, 1992; Guillot et al., 2009) as well as experimental phase relations (Evans et al., 1976; Ulmer & Trommsdorff, 1995; Wunder & Schreyer, 1997) confirm that serpentine group minerals are present in both the subducting slab and mantle wedge. As the hydrated slab subducts into the mantle, H_2O-rich fluids are driven off into the overriding plate (Schmidt & Poli, 1998), thus contributing to the serpentinization of the forearc. Consequently, serpentinites play a key role in the generation of arc magmas (e.g., Grove et al., 2009) and the global water cycle (Magni et al., 2014; Rüpke et al., 2004). The effects of serpentine minerals on the mechanics of the subduction zone system are still debated (Reynard, 2013). It has been suggested that serpentine may contribute to episodic tremor and slip/slow slip events (Abers et al., 2009; Hilairet et al., 2006; Kaproth & Marone, 2013), intermediate-depth earthquakes (Hacker et al., 2003; Jung et al., 2004), and the apparent weakness of the subduction interface (Hirauchi et al., 2010; Hyndman et al., 1997; Peacock & Hyndman, 1999).

In addition to the potential effects listed above, serpentine group minerals have also been observed to have a distinct seismological signature (Christensen, 2004). All serpentine group minerals are slow to seismic waves (Bezacier et al., 2010; Horen et al., 1996). Single crystals of antigorite—the high temperature, high-pressure structure of the serpentine group—have also been shown to be extremely elastically anisotropic (66% anisotropic to *S* waves) (Bezacier et al., 2010, 2013; Marquardt et al., 2015).

Over the last 30 years, shear wave splitting has been used to map out seismic anisotropy in the mantle and infer from these measurements the deformation conditions inside the earth (Savage, 1999). In subduction zones, where deformation conditions are complex, there has been much debate over the origins of both mantle wedge and subslab trench-parallel *S* wave splitting (see Long and Wirth, 2013, and references therein). It has been proposed that the anisotropy of antigorite could account for these observations of shear wave splitting at subduction zones that are difficult to explain by olivine anisotropy alone (Bezacier et al., 2013; Jung, 2011; Katayama et al., 2009; Marquardt et al., 2015).

Observations of seismic anisotropy in the mantle are commonly used to infer patterns of flow in the upper mantle by assuming they are the direct result of deformation of an anisotropic material (e.g., Long & Wirth, 2013, and references therein). However, antigorite can also form anisotropic fabrics as it forms from olivine by nucleation and growth that occurs in preferential crystallographic orientations, a phenomenon known as topotaxy (Boudier et al., 2010; Morales et al., 2018). This introduces further uncertainty into the interpretation of seismic anisotropy in subduction zones by removing the direct link between deformation of the anisotropic medium and the associated observations of seismic anisotropy at the surface.

In order to better understand the influence of mantle serpentinization on deformation and how the presence of both deformed and topotactic microstructures in antigorite affects seismic anisotropy in subduction zones, four partially serpentinized rocks were selected for analysis from the mantle section of the Kohistan palaeo-island arc complex. The samples were investigated using electron microscopy and electron backscatter diffraction (EBSD) to determine the relationships among serpentinization, deformation, and the associated seismological properties (Figure 1).

2. Methods

2.1. Samples and Locations

The suite of rocks selected for analysis is from the ultramafic part of the Sapat Complex in northern Pakistan (Jan et al., 1993). This peridotite body is a rare fragment of subarc mantle belonging to the Kohistan-Ladakh Palaeo-island arc (Bouilhol et al., 2009), one of only two examples globally of subarc mantle exposed at the surface (Mehl et al., 2003). The Sapat peridotite is a 12×1 km sized body of metaharzburgites, dunites, pyroxenites, and metagabbros in the hanging wall of the Indus Suture Zone (Figure 2). Field relations, microtextures, bulk, and mineral chemistry document the formation of a crust-mantle transition zone at the expense of metaharzburgites by melt-rock reactions and melt fractionation producing dunites and olivine-clinopyroxenites from the same melt type. Uncommon vein assemblages in the dunites that include Cr-clinochlore, calcite, and olivine document a late percolation of slab-related, volatile-rich fluids (Bouilhol et al., 2012). Considering the highly refractory composition of the Sapat mantle, its structural position, the evidence for interaction with highly depleted arc melts, and the subsolidus interaction with volatile-rich

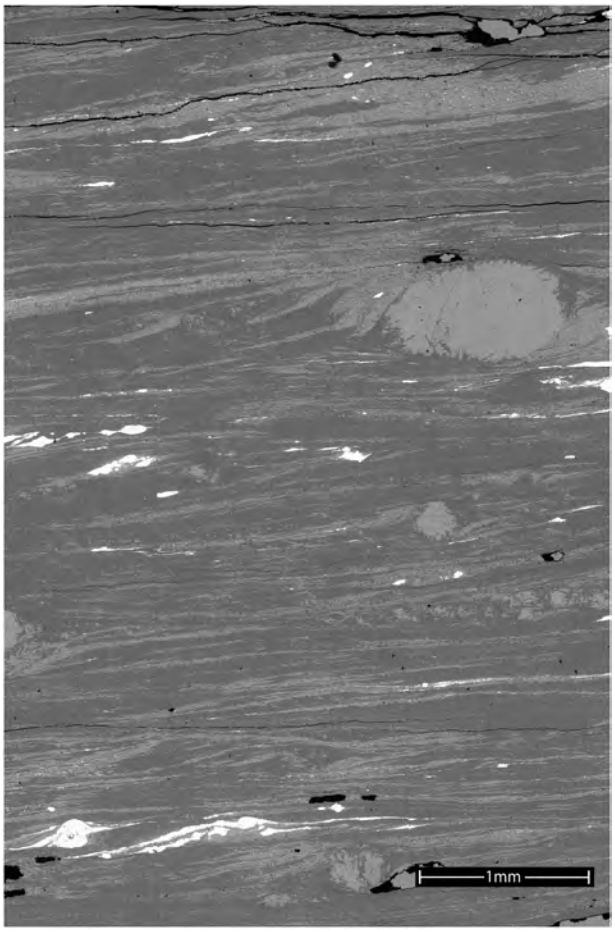

Figure 1. Stitched backscatter electron image of sample D3. Maps such as this one were used for the determination of phase proportions by thresholding the image into four distinct colour ranges: black = holes, dark grey = antigorite, light grey = olivine, white = magnetite.

arc fluids, the Sapat ultramafic rocks are interpreted as being derived from the frontal Kohistan Arc (Bouilhol et al., 2012, 2009; Burg, 2011). The arc mantle section of Sapat has recorded two main phases: (1) magmatic activity and evidence for melt transfer (Bouilhol et al., 2011) followed by (2) a subsequent cooling and hydration (serpentinization) of the fore-arc ultramafic rocks by a Tethyan slab-derived fluid (Bouilhol et al., 2012). As such the ultramafic rocks of Sapat have been used to investigate fore-arc mantle processes including fore-arc serpentinization (e.g., Debret et al., 2018).

The sample set includes both highly deformed mylonites and more moderately deformed tectonites. The locations of the samples used in this study can be seen in Figure 2 (see also Bouilhol et al., 2009). From a larger suite of Kohistani specimens, four specimens were selected for EBSD analysis: three mylonites and one minimally deformed sample (henceforth, the "protomylonite"—Table 1). All four rocks are dunites that have been largely altered to antigorite. Minor magnetite, pyroxene, and chlorite are also present. The mylonites all display a very strong crystallographic alignment of the antigorite grains, as is evidenced by similar angles of extinction across an entire thin section when viewed optically in crossed-polarised light (Figure 3). Furthermore, the protomylonite (D9) consists of cores of relict olivine grains surrounded by haloes of antigorite grains. These surrounding antigorite grains are arranged into domains that appear to have some degree of crystallographic alignment (Figure 4).

The mylonitic samples are all fine grained, with the size of both antigorite and olivine grains between 1 and 10 μm. All three mylonites bear large (~100 μm to 1 mm) porphyroclasts of olivine and occasionally orthopyroxene, with larger than average antigorite grains in the strain shadows of the relict grains. There is some variation between samples in the percentage of porphyroclasts and the extent to which the minerals in the sample are layered or well mixed (Table 1 and Figure 3). Phase proportions (Table 1) were estimated from backscatter electron image maps of the thin section surface using the software package ImageJ (Figure 1).

In contrast to the mylonitic samples, the protomylonite (D9) is relatively coarse grained, with millimeter-scale olivine grains and well-formed antigorite grains on the order of 100 μm long.

2.2. EBSD and Postprocessing

To perform microstructural analysis, thin sections were prepared for each specimen. Samples D3 and D6 exhibit a well-defined foliation and lineation; thin sections were oriented perpendicular to the foliation and parallel to the lineation. Sample D96 is foliated but does not show clear evidence for a lineation so the thin section was only orientated with respect to the foliation. The protomylonite (D9) does not display any clear indicators of prior deformation in hand specimen and was therefore cut in three orthogonal directions that were each analysed in order to avoid any orientation bias.

Thin sections were polished to EBSD standards with a final step of colloidal silica on a Vibromet polisher for 3 hr. Uncoated thin sections were examined under low-vacuum conditions (20–30 Pa) using a JEOL 7001LVF FE-scanning electron microscope equipped with Oxford Instruments' Symmetry EBSD Detector. Several match units were evaluated to index the antigorite. The best results were obtained using a match unit for monoclinic antigorite created from the atomistic calculations of Capitani and Mellini (2004). This crystal structure has a comparatively long *a* axis (43.505 Å), which is consistent with a metamorphic temperature of approximately 435 °C (Mellini et al., 1987). Indexing rates were generally low and ranged between 13% and 63%. Map areas ranged between 2.765 and 63.806 mm^2. This is inferred to be due to the difficulty in achieving an ideal surface polish (Inoue & Kogure, 2012), especially among the finer grained specimens. A

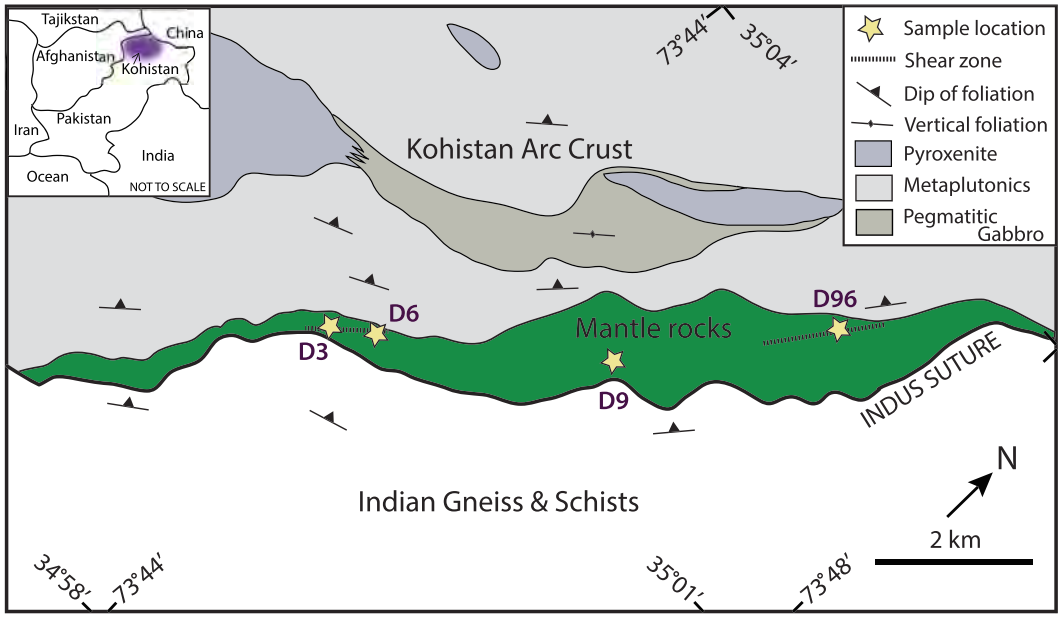

Figure 2. Simplified geologic map of the Sapat peridotite, NW Pakistan, an approximately 12 × 1 km sized body of subarc mantle in the hanging wall of the Indus suture. Kohistan is denoted by the purple region in the inset map. Locations of samples used in this study are marked with yellow stars. Modified from Bouilhol et al. (2009).

maximum of 7 bands were detected and up to 50 reflectors used for indexing with a Hough space resolution of 105 (following the recommendations of Brownlee et al., 2013).

EBSD maps were created by rastering the beam with step sizes of 7.7–25 μm. Due to the small grain size of the mylonites, the step size was selected to be greater than the grain size so that each individual data point represented the orientation of a single grain. The relatively coarse resolution of the map enabled the collection of large sets of unique grain orientations. However, a potential consequence of this coarse mapping scheme is that misindexed points will introduce some random noise into the orientation data. As such the strength of the LPO reported in this study is considered to be a lower limit. In contrast, the protomylonite, which has larger grains, was mapped at a resolution whereby each grain was sampled multiple times.

Table 1
Samples Investigated in This Study

Sample	Location	Microstructure	Mineralogy	Ant:Ol (normalized areal %)
Mylonites				
D3	35°00′54.1″N 73°43′62.0″E	Ant and ol (~1–10 μm), few ~100 μm ol and opx porphyroclasts, foliated with mgt lineation	Ant, ol, mt + opx	74:26
D6	35°00′77.9″N 73°43′96.5″E	Ant and ol (~1–10 μm), few ~100 μm ol and opx porphyroclasts, mgt lineation	Ant, ol, mt + opx	64:36
D96	35°03′21.9″N 73°46′81.1″E	Ant and ol (~10 μm), ~1 mm ol and mgt porphyrolasts, foliated	Ant, ol, mt	67:33
Protomylonite				
D9	35°01′72.1″N 73°45′39.7″E	Altered ol (~1 mm), new ant (~100 μm) preserves old ol domains	Ant, ol, mt, cpx, chl	70:30

Note. Abbreviations are as follows: ant = antigorite; ol = olivine; opx = orthopyroxene; mt = magnetite; cpx = clinopyroxene; chl = chlorite.

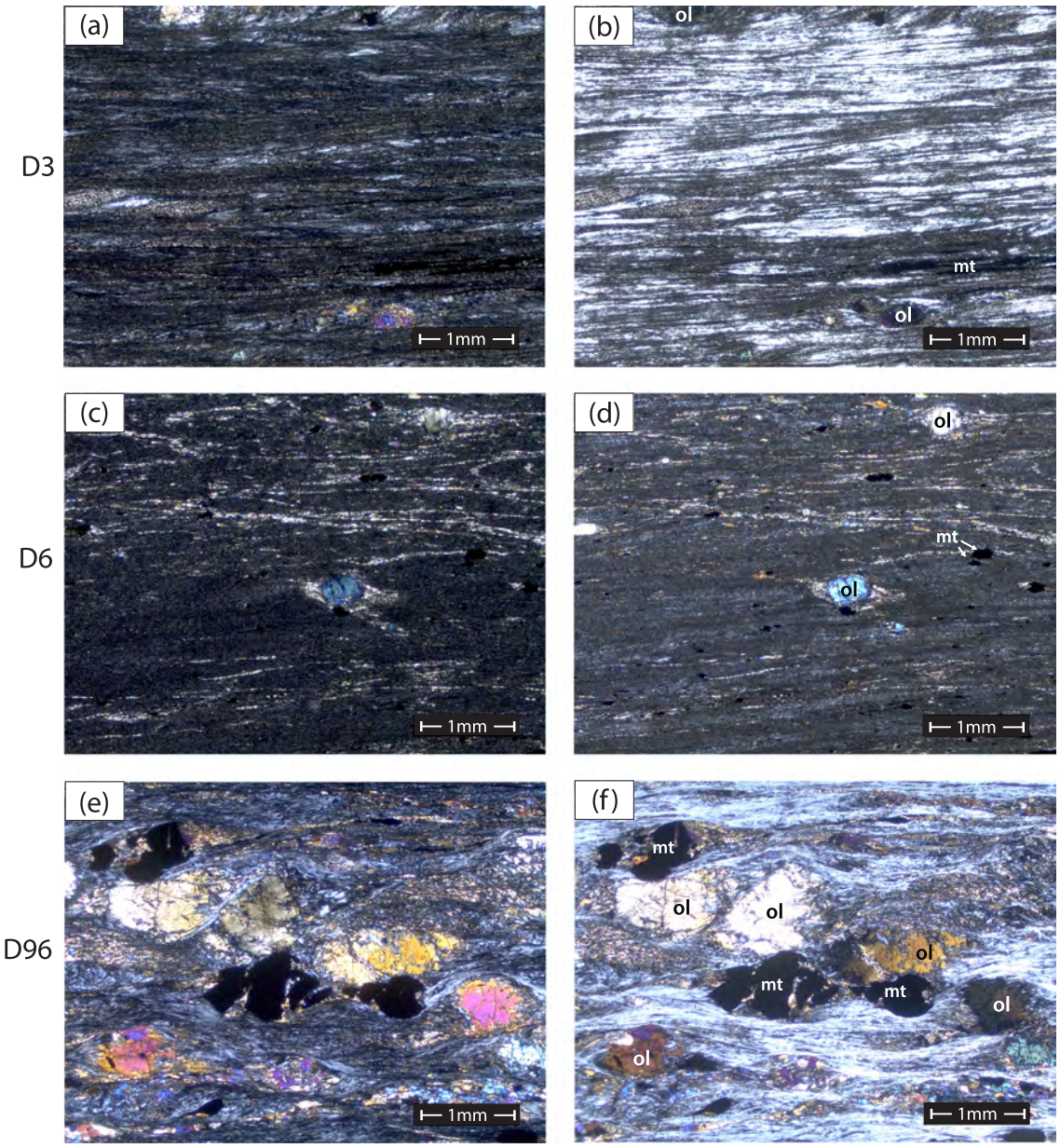

Figure 3. Photomicrographs in crossed-polarized light of the three mylonitic samples (D3, D6, and D96). The panels on the left (a, c, e) and right (b, d, f) display the same field of view but with the polarizers rotated by 45°. Low birefringence (grey to white) grains are antigorite, opaque grains are magnetite, and higher birefringence (orange, pink and purple) grains are olivine. Fine-grained olivine appears dark and occluded. It can clearly be seen that there is a strong crystallographic alignment of the antigorite grains, since all become extinct at roughly the same angle. Larger grains are labeled by mineralogy: ol = olivine, mt = magnetite.

Postprocessing of EBSD data was performed using the MATLAB toolbox MTEX, version 5.1.1. (Bachmann et al., 2010, 2011; Hielscher & Schaeben, 2008; Mainprice et al., 2015). The seismic properties were computed with the script written by Mainprice et al. (2011) using the elastic tensors of Abramson et al. (1997) (olivine) and Bezacier et al. (2010, 2013) (antigorite) at ambient pressure and temperature. A Voigt-Reuss-Hill averaging scheme was employed. For consistency, all orientation distribution function calculations were computed using a de la Vallée Poussin kernel and half widths of 15°. Calculations were performed on antigorite-only end member and specimen specific mixtures of antigorite and olivine. Models of seismic anisotropy were computed directly from the raw EBSD data without application of any smoothing algorithms.

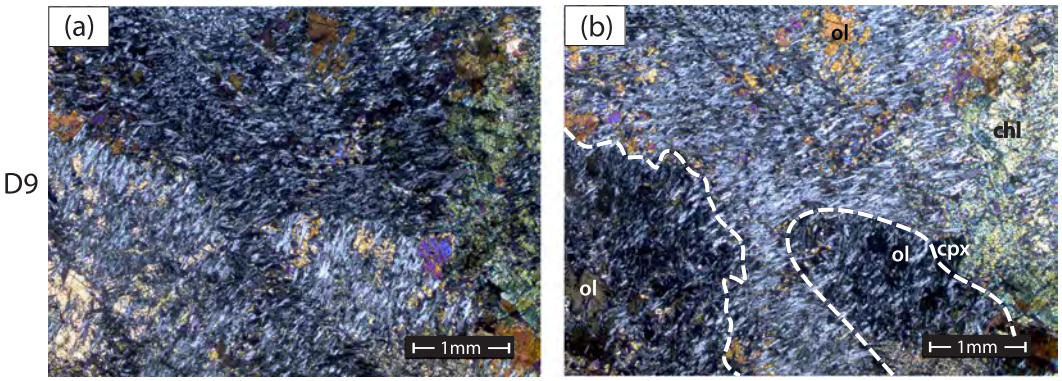

Figure 4. Photomicrographs in crossed-polarized light of the protomylonitic sample (D9). (a) and (b) display the same field of view but with the polarizers rotated by 45°. Low birefringence (grey to white) grains are antigorite, and higher birefringence (orange, pink, and purple) grains are olivine. Relict cores of olivine can be seen surrounded by haloes of antigorite which become extinct at roughly the same angle, suggesting some degree of crystallographic alignment (outlined in white dashed lines in panel b). Larger grains are labeled by mineralogy: ol = olivine, mt = magnetite, chl = chlorite, cpx = clinopyroxene.

Percent S wave anisotropy is presented as peak-to-peak anisotropy: $k = 200 * (V_{S1} - V_{S2})/(V_{S1}+V_{S2})$, where V_{S1} and V_{S2} represent the fastest and slowest S wave directions, respectively, through the whole rock.

3. Results

3.1. Crystallographic Orientation

The antigorite grains in the three mylonites (Figure 5) display a consistently strong texture with the (001) planes oriented parallel to the plane of the mylonitic foliation. In samples D3 and D96, this is accompanied by strong point maxima in the poles to the (100) and (010) planes, with (010) poles parallel to the lineation and (100) poles perpendicular to the lineation in the plane of the foliation. This relationship is harder to determine for sample D6, where the (100) and (010) poles appear to be more girdled. This orientation is consistent with the "B-type" antigorite LPO described by Nishii et al. (2011). This LPO could be explained by the activation of the [010](001), as reported by Auzende et al. (2015) and Padrón-Navarta et al. (2012). However, in order to confirm this as the dominant slip system, a much more detailed microstructural study would have to be performed. Nonetheless, this is inconsistent with the antigorite slip systems suggested by Amiguet et al. (2014) and Van De Moortèle et al. (2010), who both reported apparent dominant slip systems of [100](001). As in Nishii et al. (2011), there is trend in the relative strengths of the microstructure with increasing percentage of antigorite, with sample D3 containing the highest volume percent of antigorite and having the strongest clustering of crystal axes and sample D6 having the lowest percent antigorite and exhibiting the weakest LPO (Figure 5).

In comparison, the olivine (Figure 6) has a weaker LPO. In both sample D3 and sample D6 there is a weak point maximum of the [010] axes perpendicular to the foliation plane; this is not detected in sample D96.

The EBSD results of the olivine grains (Figure 7b) in the protomylonite reveal a weakly orthogonal microstructure. Without any indicators of a shear sense, it is impossible to classify this microstructure according to the framework of Jung et al. (2006), other than to say that this sample has likely experienced some small amount of deformation. Additionally, the LPO of the antigorite grains in this sample (Figure 7a) is much weaker than the microstructures seen in the mylonites, with faint girdles seen in the poles to the (100) and (010) planes.

3.2. Stacked Protomylonite

Orientation data were analysed to test for topotaxy by evaluating the crystallographic relationship between adjacent grains of olivine and antigorite. In total, 690 olivine grains and 12,267 antigorite grains were analysed in this way. To identify common relationships between olivine grains with different orientations, all data were rotated and stacked. Each olivine grain was rotated into a single orientation, and all spatially

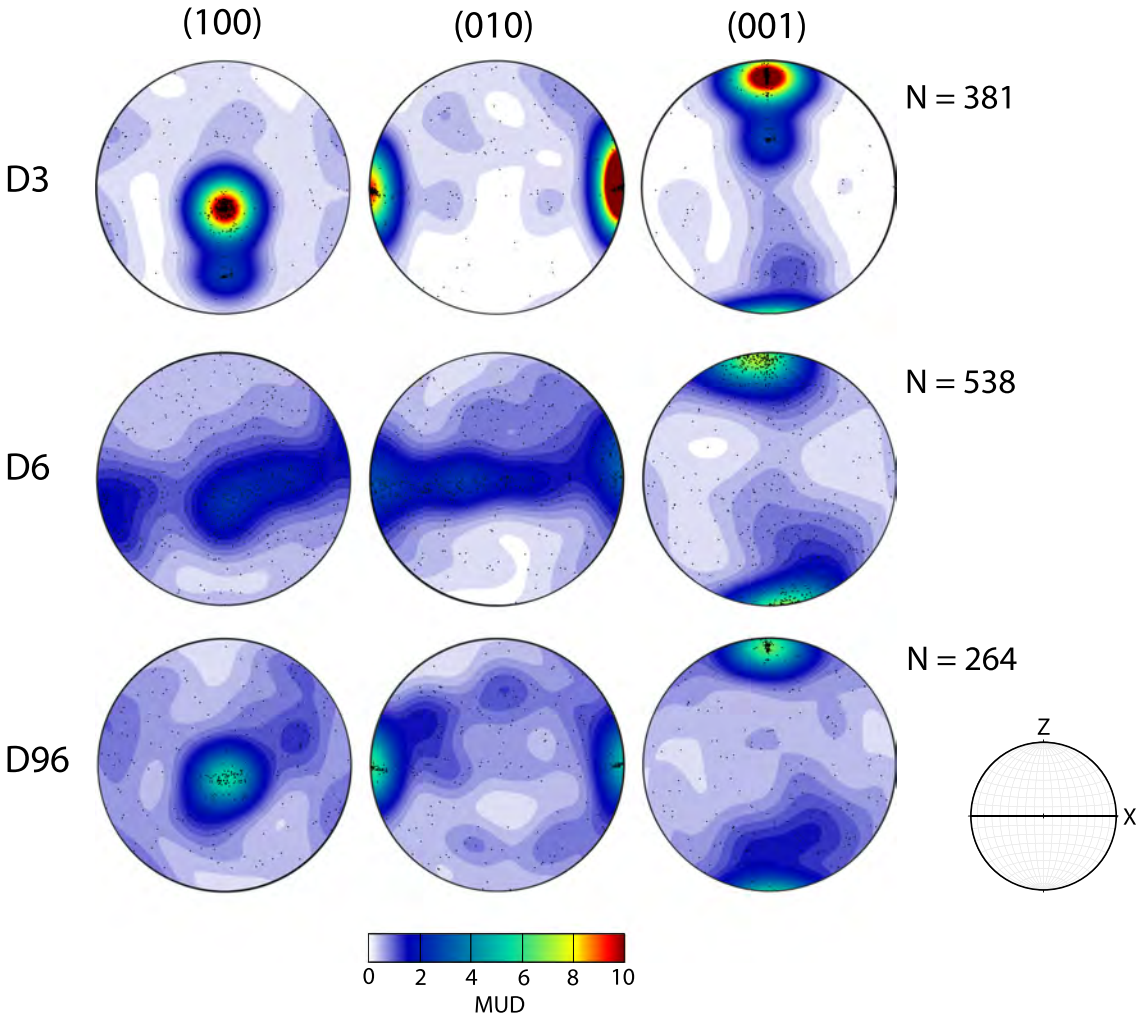

Figure 5. Pole figures of antigorite from the three mylonitic samples plotted in a lower hemisphere, equal area projection. The pole figures are coloured according the multiples of a uniform distribution (MUD) with individual grains plotted on top as black points. *N* is the number of grains sampled to create each set of pole figures. The small stereonet to the lower right-hand side shows the orientation of the shear plane (black line) with the lineation denoted by *X*. The normal to the shear plane is *Z*. All three samples display similar LPOs, characterized by the poles to the (001) planes perpendicular to the shear plane and the poles to the (010) planes parallel to the lineation.

associated antigorite grains were subjected to the same rotation. Figure 8 shows the orientation of the stacked antigorite data. These pole figures show clearly that there is a nonrandom orientation relationship between olivine and antigorite grains.

There are two antigorite-olivine relationships present in sample D9. In both these relationships, (010)ant//(100)ol is a dominant feature. As in Morales et al. (2018), we observe (010)ant//(100)ol with [100]ant//[001]ol. We also observe a peak of olivine [010] axes near to antigorite [100]. The calculated directions in contact are [13 0 $\bar{1}$]ant//[010]ol, which is very nearly equivalent to [100]ant//[010]ol. Given that this calculation assumed antigorite to be orthorhombic ($\alpha = \beta = \gamma = 90°$) whereas in reality $\beta = 91.32°$ (Capitani & Mellini, 2004), the comparatively long length of the *a* axes in antigorite (43.505 Å) will cause this approximation to break down for planes parallel to (100). Therefore, we take these relationships to be (010)ant//(100)ol and [100]ant//[010]ol. We estimate that the proportion of the grain boundary length that is characterized by these relationships is ~15%, respectively. A summary of other topotactic relationships that have been observed in prior studies is shown in Table 2. We did not observe a significant contribution from any of these other crystallographic relationships, save (010)ant//(100)ol & [100]ant//[001]ol as reported by Morales et al. (2018).

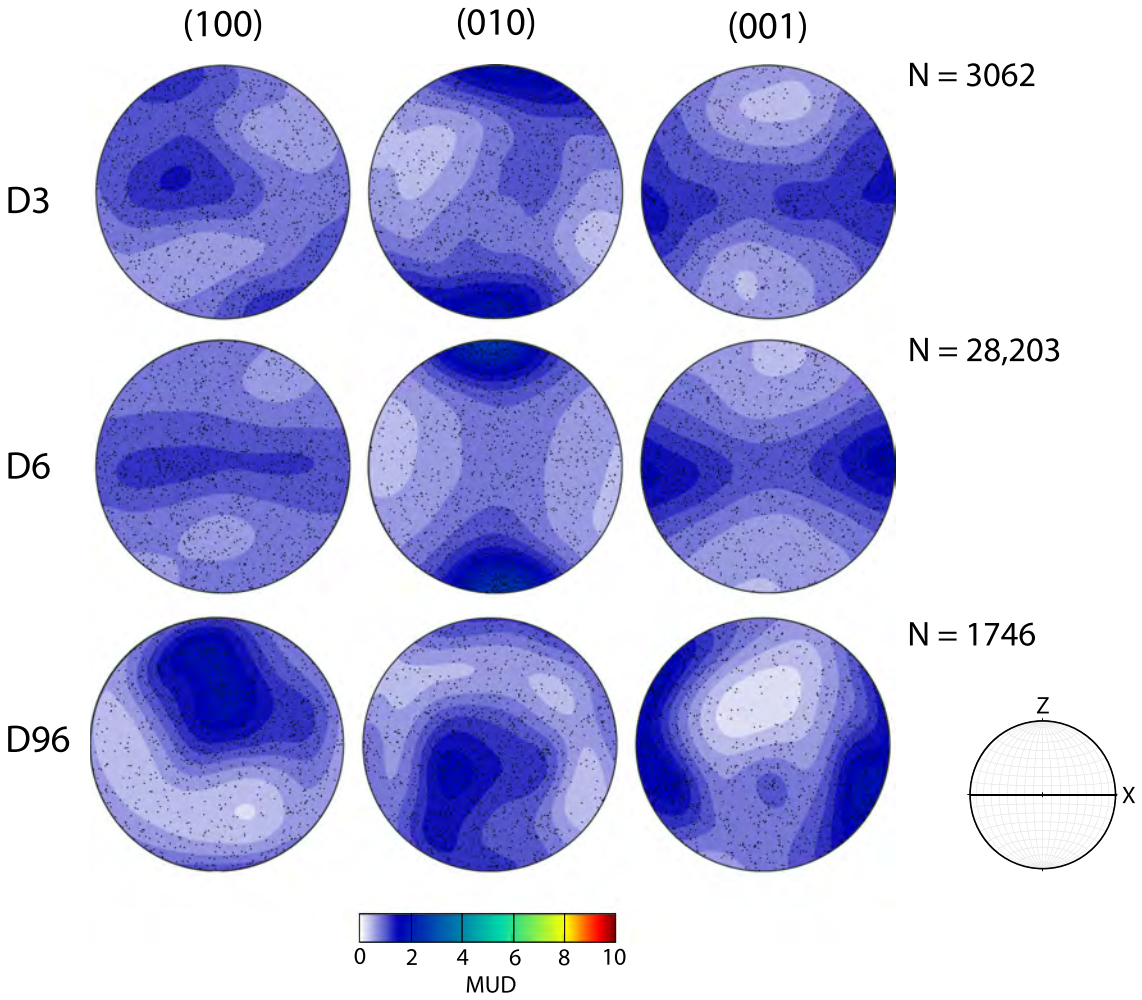

Figure 6. Pole figures of olivine from the three mylonitic samples plotted in a lower hemisphere, equal area projection. The pole figures are coloured according the multiples of a uniform distribution (MUD) with individual grains plotted on top as black points. *N* is the number of grains sampled to create each set of pole figures. The small stereonet to the lower right-hand side shows the orientation of the shear plane (black line) with the lineation denoted by *X*. The normal to the shear plane is *Z*. None of the three samples have well-aligned olivine crystals, but samples D3 and D6 appear to have some clustering of the [010] axes perpendicular to the shear plane.

4. Discussion

4.1. Seismic Anisotropy in Subduction Zones

Patterns of upper mantle flow are commonly interpreted by assuming simple relationships among deformation of olivine, the resulting LPO, and the consequent seismic anisotropy (Karato et al., 2008; Skemer & Hansen, 2016). While models of LPO evolution reproduce seismological observations with reasonable accuracy when considering the relatively simple deformation conditions beneath the centers of oceanic plates (Becker et al., 2014), these same models are unable to reproduce observations in more complex kinematic environments (Skemer et al., 2012). In subduction settings, large trench-parallel *S* wave delay times (>1 s) have been explained by changes in olivine microstructures caused by the increased levels of water in the mantle wedge (Kneller et al., 2008). However, experiments and natural samples suggest that peak-to-peak *S* wave anisotropy in deformed peridotites is between 1.1% and 14.6% (Jung, 2018; Mainprice et al., 2000). Even if the whole of the mantle wedge was uniformly anisotropic in this way, it is difficult to accumulate the observed splitting times from olivine microstructures alone (Katayama et al., 2009). Several authors (Bezacier et al., 2010, 2013; Brownlee et al., 2013; Jung, 2011; Katayama et al., 2009) have suggested that antigorite may contribute to the observations of shear wave splitting in the mantle wedge.

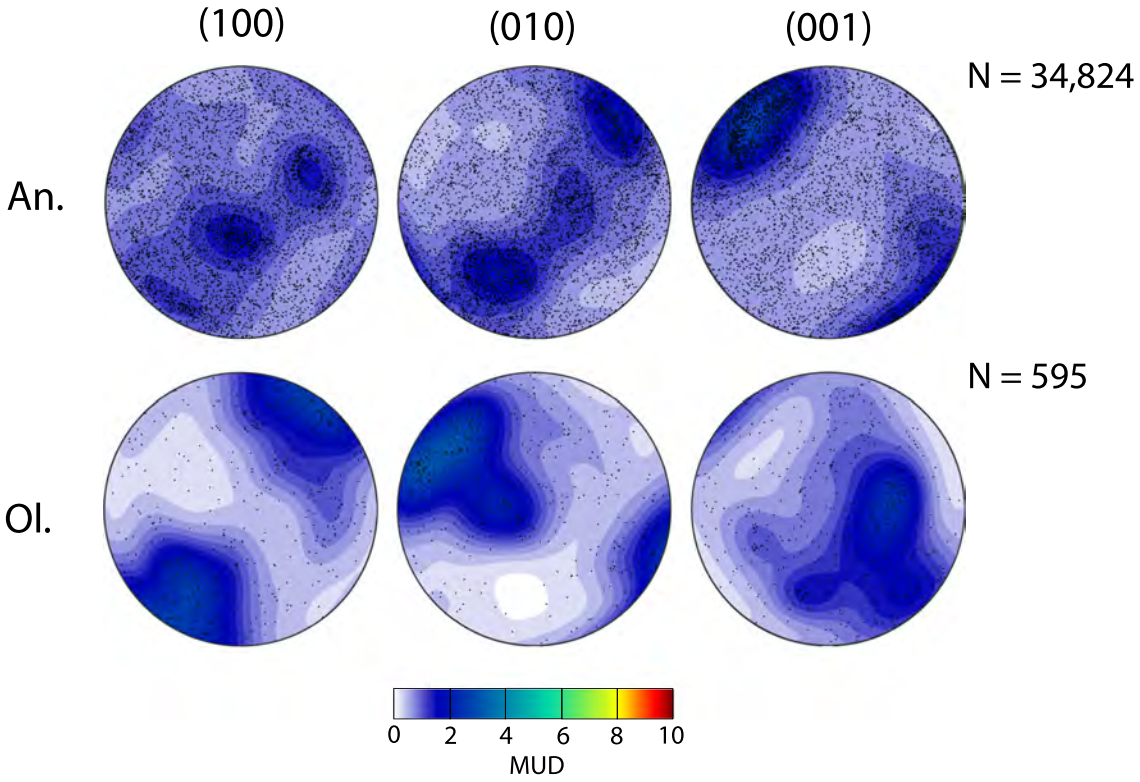

Figure 7. Equal area, lower hemisphere pole figures showing the bulk antigorite (top row) and olivine (bottom row) from the protomylonitic sample D9 (data from the three orthogonal sections). The pole figures are coloured according the multiples of a uniform distribution (MUD) with individual grains plotted on top as black points. *N* is the number of grains sampled to create each set of pole figures. The poles to the antigorite (001) planes roughly align with the olivine [010] axes, with the poles to the antigorite (100) and (010) planes forming a patchy girdle. This sample was not oriented with respect to any kinematic reference frame, due to the lack of an obvious microstructural fabric.

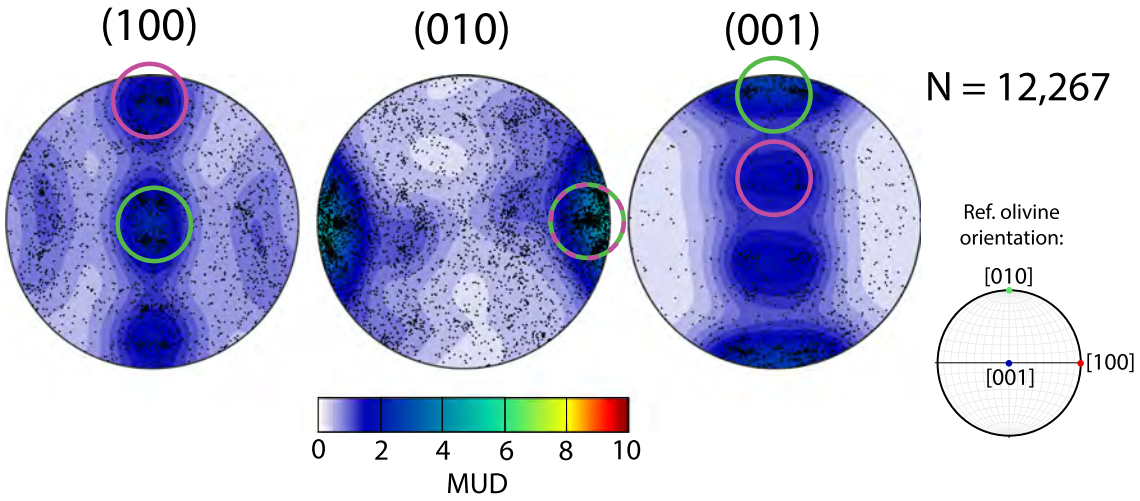

Figure 8. Equal area, lower hemisphere pole figures showing stacked antigorite grains from sample D9. Olivine grains were rotated into a reference orientation (shown in the lower right-hand corner); any antigorite grains that shared a grain boundary with this olivine were subjected to the same rotation. *N* is the number of antigorite grains sampled to create these pole figures. The pole figures are coloured according the multiples of a uniform distribution (MUD) with individual grains plotted on top as black points. Coloured circles surround the two inferred topotactic relationships: (1) (010)ant//(100)ol with [100]ant//[001]ol (green) and (2) (010)ant//(100)ol with [100]ant//[010]ol (purple).

Table 2
Topotactic Relationships Reported for the Reaction Olivine + H_2O ➔ Antigorite

Planes	Directions	Reference
(001)ant//(100)ol	[010]ant//[001]ol	Boudier et al. (2010) and Morales et al. (2013)
(001)ant//(010)ol	[010]ant//[001]ol	Boudier et al. (2010) and Morales et al. (2013)
(210)ant//(010)ol	[001]ant//[100]ol	Morales et al. (2018)
(010)ant//(100)ol	[100]ant//[001]ol	Morales et al. (2018) and this study
(010)ant//(100)ol	[100]ant//[010]ol	This study

To understand how the presence of antigorite affects observations of shear wave splitting, we calculated the seismic anisotropy for each mylonite sample (Figure 9) using the code written by Mainprice et al. (2011). For the strongest mylonitic antigorite fabric (D3, Figure 9a), the fastest *P* and *S* wave directions lie within the shear plane. When the data are rotated to simulate looking down into the shear plane, appreciable shear wave splitting that is perpendicular to the shear direction (*X*) only occurs when there is a relatively small angle (less than ~30°) between the raypath and the shear plane. The strongest antigorite microstructure formed by topotaxy (Figure 9b) generates a much weaker anisotropy in comparison to the mylonitic antigorite. It also does not appear from this figure to exhibit significant variation in the orientation of shear wave splitting.

For sample D3, which exhibits the strongest texture and hence represents an upper bound on the magnitude of anisotropy generated by an antigorite-rich rock, we calculate the three-dimensional effect of the sample orientation on the passage of a vertically incident *S* wave (Figure 10). Sample orientation is defined with respect to the shear plane (plane normal to *Z*) and shear direction (*X*), which are assumed to be parallel to the sample foliation and lineation, respectively. These models also assume that antigorite is the sole phase present in the sample and that the shear direction is perpendicular to a hypothetical subduction zone trench. In Figure 10a, colours correspond to the angle between the shear direction (*X*) and the horizontal projection of the orientation of the fast *S* wave. Values approaching 90° correspond to splitting that is trench parallel; values approaching 0° correspond to splitting that is trench normal. These calculations reveal that under many conditions, antigorite microstructures can produce *S* wave splitting that is parallel or subparallel to the trench. The maximum delay time for trench-parallel splitting is achieved when the shear plane is dipping at greater than ~70° from horizontal (i.e., rotation about the *Y* direction is greater than ~70°). It is also possible to generate smaller splitting times with the fast direction at an angle oblique to the trench for more shallowly dipping shear planes and/or for shear planes that are rotated about the shear direction.

We performed similar calculations exploring the maximum shear wave splitting signature of antigorite formed by topotactic substitution, rather than by deformation. Figure 11 shows that for the same model assumptions, the maximum delay time is only ~25% of the maximum delay time generated by the mylonite.

Table 3
Vp and Vs Anisotropy Values for Samples in This Study

Sample	*Vp* anisotropy (%)	Max. *Vs* anisotropy (%)	*Vp* anisotropy (%)	Max. *Vs* anisotropy (%)
Antigorite			Antigorite + Olivine	
D3	34.2	43.3	24.7	30.9
D3 (Voigt)	34.6	40.8	21.5	23.9
D3 (Reuss)	33.9	46.5	28.4	39.8
D6	22.3	27.2	14.3	17.7
D96	17.4	18.2	12.1	12.3
D9 (bulk)	9.5	9.6	8.0	8.0
D9 (stacked)	13.7	11.8	—	—
Bezacier et al. (2010) single crystal antigorite			Polycrystalline antigorite	
	46	66	37	50
Olivine				
D6	2.7	1.7	—	—

Note. All calculations are VRH averages unless otherwise specified. See Bezacier et al. (2010) for details on the single crystal and polycrystalline antigorite measurements.

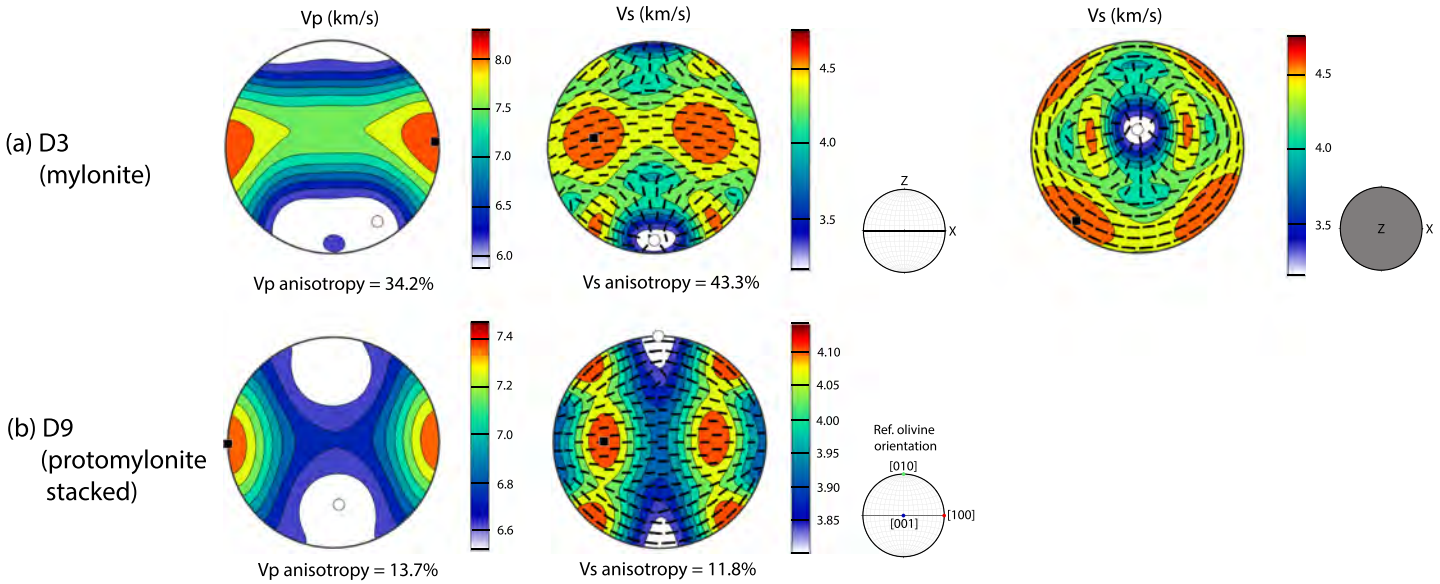

Figure 9. Pole figures showing the seismic wave speed as a function of direction in equal area, lower hemisphere projections. (a) Seismic wave speeds (*Vp* and Vs_1 (the fast *S* wave polarization)) of the antigorite from the strongest mylonitic fabric (sample D3—compare with Figure 5). The plot to the furthest right shows the *Vs* data again, rotated by 90° about the *X* direction, as though looking down into the shear plane. Black bars overlying the Vs_1 plot indicate the polarization direction of the faster *S* wave. (b) Seismic signature of the stacked antigorite (compare with Figure 8) from the nominally deformed sample D9. This is the upper limit to the seismic anisotropy that could be generated by a topotactic substitution. In particular, the *P* wave anisotropy calculated for the topotactic overgrowth is around 1.5–2.5 times weaker than the *P* wave anisotropy calculated for the mylonites. Similarly, the *S* wave anisotropy for this theoretical maximum topotactic microstructure is 2–3.5 times weaker than the *S* wave anisotropy for the mylonites. Therefore, a thickness on the order of 100 km of the topotactic antigorite found in this sample (D9) would be required to generate splitting times on the order of 1 s. Along with olivine microstructures, the anisotropy generated by the topotactic microstructures is too weak to account for a large proportion of observed trench-parallel anisotropy without making assumptions that are geologically unreasonable.

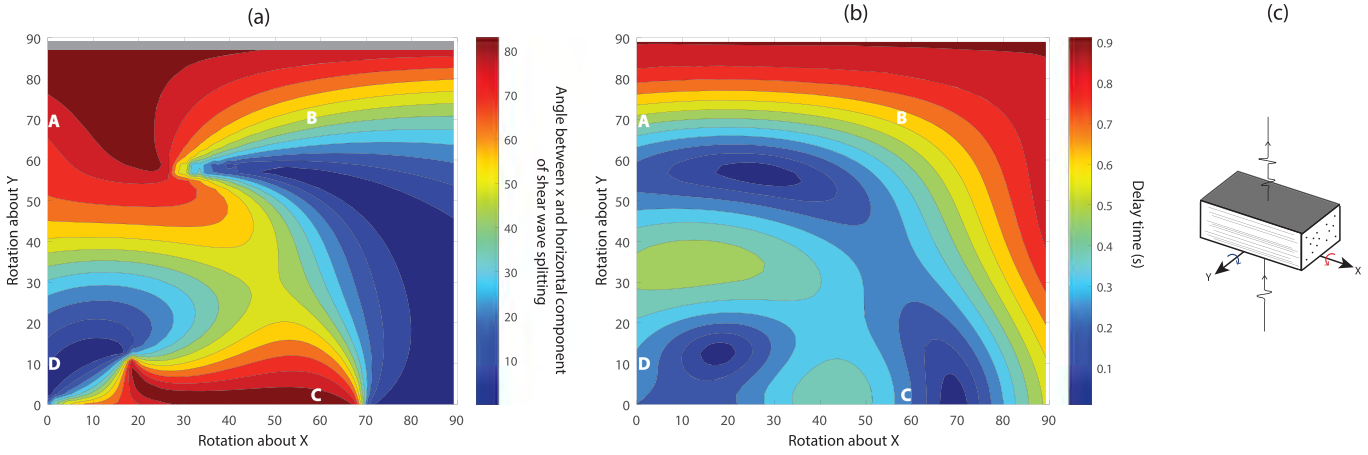

Figure 10. The 2-D representation of the 3-D effect of the antigorite with the strongest LPO (D3) on a vertically incident *S* wave, after Skemer et al. (2012, their Figure 5). A thickness of 10 km was used, and in all calculations it was assumed that antigorite was the only phase present. A–D correspond to the four hypothetical raypaths shown in Figure 12. Rotations about *X* and *Y* from 0° to 90° can be visualized as a progressively more steeply dipping foliation plane with a strike that is either parallel to the direction of plate motion (*X*) or to the strike of the trench (*Y*), assuming orthogonal convergence. (a) Contour plot showing the change in angle between the polarization direction and the horizontal component of the shear direction (*X*) as the sample is rotated about *X* and *Y*. Colours range from blue (trench-perpendicular fast directions) through to red (trench-perpendicular fast directions). The greyed-out region corresponds to the model space where the vertical raypath is parallel to *X* and thus the angle between *X* and the horizontal component of the splitting is undefined. (b) Contour plot showing the effect of sample orientation on the magnitude of the delay time. Due to the symmetry of the effects, only part of the full angular spectrum is presented. Colours range from blue (minimal delay times) to red (large delay times). (c) Schematic showing how the sample (lines = foliation, dots = lineation, grey region = shear plane) is rotated with respect to the incoming *S* waves (thin arrow).

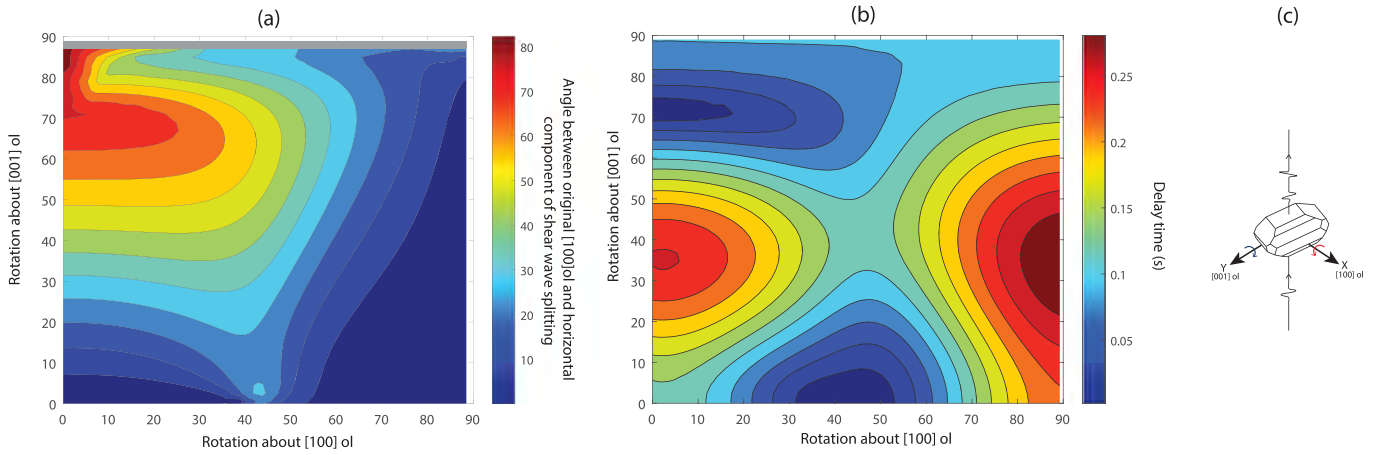

Figure 11. The 2-D representation of the 3-D effect of the stacked antigorite from the protomylonitic sample (Figure 8) on a vertically incident *S* wave, after Skemer et al. (2012, their Figure 5). This is the hypothetical strongest signature which can be generated from an antigorite serpentinite which developed as a result of the topotactic growth described herein. A thickness of 10 km was used, and in all calculations it was assumed that antigorite was the only phase present. "Horizontal component of shear wave splitting" refers to the calculated split projected into the original *X*-*Y* plane. (a) Contour plot showing the change in angle between the polarization direction and the horizontal component of the shear direction (*X*) as the sample is rotated about *X* and *Y*. Colours range from blue (fast directions parallel to *X*) through to red (fast directions parallel to Y). The greyed-out region corresponds to the model space where the vertical raypath is parallel to [100]ol, and thus, the angle between [100]ol and the horizontal component of the splitting is undefined. (b) Contour plot showing the effect of sample orientation on the magnitude of the delay time. Due to the symmetry of the effects, only part of the full angular spectrum is presented. Colours range from blue (minimal delay times) to red (large delay times). (c) Schematic showing how the original olivine crystal is rotated with respect to the incoming *S* waves (thin arrow).

In addition, in order to generate trench-parallel splitting with measurable delay times, the original [100] axes of the olivine would have had to have been parallel to the trench prior to the reaction which formed the antigorite. Olivine microstructures with the [100] axes parallel to the trench are generally interpreted as occurring due to elevated water contents in the wedge resulting in a change in olivine slip systems (Kneller et al., 2008) or patterns of mantle flow which run parallel to the trench (Mehl et al., 2003). These phenomena can explain trench-parallel *S* wave anisotropy without considering the presence of antigorite. If topotactic growth of antigorite is occurring in areas affected by either of these processes, it is possible that the small amount of anisotropy afforded by the presence of the topotactic antigorite could add to any anisotropy from the olivine microstructures. However, this effect would be minor and not distinguishable seismologically.

While this study and others have confirmed that topotactic substitutions occur during the hydration of peridotite, the textures produced by this process are weak and are therefore unlikely to modify existing interpretations of anisotropy. Significant contributions to subduction zone anisotropy will only occur if a peridotite metamorphosed to serpentinite is subsequently deformed.

4.2. Interpretation of 3-D Seismic Signature

As a preliminary framework with which to interpret these data, we assume that the downgoing slab induces shear on a narrow band of antigorite in the mantle wedge that is parallel to the slab surface. It should be noted that no subducting slab exceeds a dip of 70° close to the trench (Syracuse et al., 2010). Moreover, few subduction zones exhibit significant along-strike changes in dip that might induce some rotation of the antigorite texture about the shear direction (*X*). However, not all *S* wave raypaths used in studies of anisotropy at subduction zones are exactly vertical, with many studies taking waves from a cone with an incidence angle of less than 30° (see Long & Wirth, 2013, and references therein). Consequently, an *S* wave that traverses the shear plane at an angle less than vertical could easily achieve shallow angles relative to the slab geometry that are sufficient to produce these patterns. For example, a local earthquake occurring in a slab which dips at 60° from the horizontal (e.g., Nicaragua) will generate raypaths in a variety of directions (Figure 12). An *S* wave that leaves the source at an angle of 20° from the slab surface and arrives at the seismic station at an angle of 10° from the vertical (see raypath A in Figure 12) should be split such that the fast direction is now oriented at ~15° to the trench (assuming the sense of convergence is trench normal). The magnitude of the splitting time should be large—~0.5 s for a 10 km layer of antigorite. Similarly, an *S*

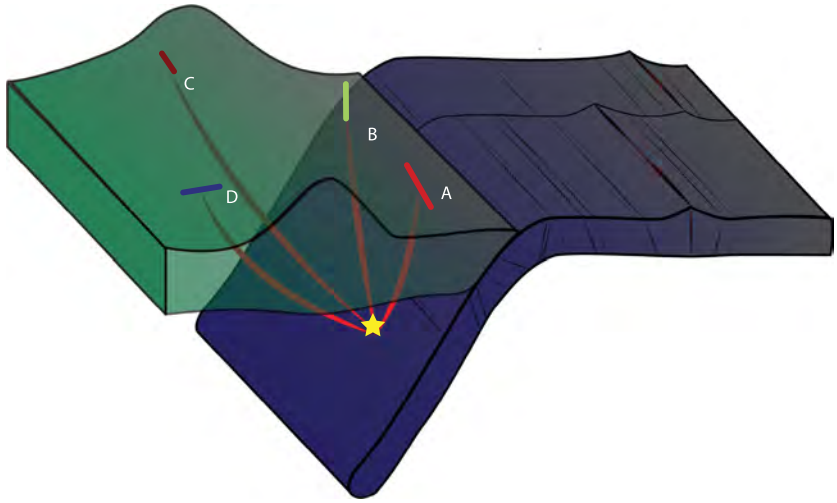

Figure 12. Schematic showing how the angle of the raypath within a subduction zone affects the magnitude and orientation of seismic anisotropy observed at a seismic station, assuming an antigorite-bearing shear plane that is parallel to the slab surface (compare Figure 10). For a local earthquake (yellow star), four different raypaths are shown. Coloured lines on the surface of the plate give the predicted fast splitting directions and relative magnitudes for a constant thickness antigorite layer that is sheared parallel to the slab surface. Colours denote the angle between the horizontal component of shear direction and the fast polarization direction (Figure 10a). The lengths of the lines are roughly proportional the magnitude of the delay times.

wave that leaves from the same source at an angle of 60° from the slab in the vertical plane (rotation about $Y = 30°$ on Figure 10) will generate a fast seismic direction that is ~30° from the shear direction. The magnitude of the splitting time in this orientation should also be ~0.5 s for a 10 km thick layer. In summary, it is plausible that the combination of a nonvertical raypath and a dipping shear zone could generate large-magnitude trench-parallel *S* wave splitting within the mantle wedge (Figures 10 and 12). It has been suggested recently that many subduction zones worldwide are too cold to fully hydrate the nose of the mantle wedge (Abers et al., 2017). However, these calculations demonstrate that only a very thin layer of deformed antigorite would be required to generate shear wave splits that are on the order of 1 s, provided that the geometry of the shear plane and the raypath are correct.

Even "typical" subduction zones exhibit complex patterns of shear wave splitting. Many authors have sought to explain these observations through the lens of complex mantle flow patterns (e.g., Nakajima et al., 2006). For example, in the Mariana and Caribbean subduction zones, trench-parallel fast directions have lead authors to conclude that there must be some component of trench-parallel mantle flow (Piñero-Feliciangeli & Kendall, 2008; Pozgay et al., 2007). Toroidal flow around slab tears and between different slabs has also been suggested (Léon Soto et al., 2009), as has oblique plate convergence (Hall et al., 2000). However, even for relatively simple deformation kinematics, the calculations presented herein could also explain the strong variability in the direction and magnitude of the *S* wave splitting observed within a single subduction zone and even a single study. If deformed antigorite is abundant within a subduction zone, it should generate a complex pattern of shear wave splitting, such as those observed by Abt et al. (2009) in Central America. Furthermore, it may be possible to explain the transition observed in some subduction zones (e.g., Tonga (Smith et al., 2001), Hikurangi (Morley et al., 2006), Mexico (Léon Soto et al., 2009), and NE Japan (Huang et al., 2011)) from trench parallel to trench perpendicular simply by considering the relationship between the raypath and the orientation of the serpentinite body (Figure 12).

4.3. Implications for the Evolution of Mantle Shear Zones

In the samples investigated herein and throughout the broader suite of samples described by Bouilhol et al. (2009), there is a strong correlation between serpentine abundance and microstructure: All the mylonites collected from this region contain abundant antigorite, whereas the undeformed rocks are relatively

unaltered. While topotaxy and weak antigorite LPOs are clearly observed in the protomylonitic sample, the mylonites themselves exhibit no discernible topotactic or epitactic signature. Therefore, we infer that any preexisting texture was overprinted by deformation. Laboratory experiments have shown that small volume fractions of serpentine can reduce significantly the strength of typical mantle rocks (Escartín et al., 2001). Moreover, the viscously anisotropic nature of serpentine (Chernak & Hirth, 2010) will promote a positive feedback between the strengthening of LPO and a reduction in shear viscosity. Due to the correlation among serpentine volume fraction, mylonitic fabrics, and antigorite LPO strength, we conclude that serpentinization and shear localisation are genetically related. Indeed, it is plausible that serpentinization enabled the initial localisation of deformation, producing zones in the mantle that are both viscously and seismically anisotropic.

5. Conclusion

Through comparison of microstructures from protomylonitic and mylonitic samples from the Kohistan arc, we show that serpentinization plays a number of important roles in the evolution of the fore-arc mantle wedge.

In the nominally undeformed protomylonitic sample, we observe at least two topotactic relationships formed during the initial stages of the serpentine reaction: (1) (010)ant//(100)ol with [100]ant//[001]ol and (2) (010)ant//(100)ol with [100]ant//[010]ol. In addition, there appears to be a girdle of directions within the plane (010)ant//(100)ol that do not fall into either directional category described above. In contrast, the mylonite samples exhibit extremely strong LPOs that are aligned with the sample foliation and are no longer related texturally with the peridotite protolith.

Modeling the seismic anisotropy reveals that antigorite in the mylonites produces extremely strong anisotropy that is on the order of tens of percent for both *P* and *S* waves. Furthermore, these microstructures are capable of generating large-magnitude *S* wave splitting when the shear plane and the incident shear wave cross at sufficiently shallow angles. This geometry may occur due to steeply dipping slabs or seismic waves that traverse the mantle wedge at shallow angles relative to the surface. Consequently, serpentinization of the fore-arc mantle can help to explain the complex patterns of *S* wave splitting observed in many subduction zones.

Stacking of the antigorite grains enabled us to calculate the maximum hypothetical seismic signature for crystallographically controlled growth. Even with this upper limit approximation, the magnitude of the anisotropy for both *P* and *S* waves is similar to the anisotropy generated by typical peridotites and is 1.5–3.5 times smaller than the anisotropy generated by the LPO in the mylonite samples. As such, deformation and overprinting of the initial antigorite LPO is needed to significantly alter the anisotropic signature of serpentinized mantle.

Therefore, serpentinization, localised deformation, and progressive LPO strengthening form a positive feedback that will affect both the rheology and seismological signature of subduction zones.

Acknowledgments
This research was supported by NSF grant EAR-1848824. Instrumentation support was provided by the Institute of Materials Science and Engineering at Washington University in St Louis. The motivation to study those samples in a microstructural framework emerged from discussions at the GeoPRISMS Subduction TEI Conference in 2015. This project has benefited from many helpful conversations with Doug Wiens and Mike Sly. We are grateful to two anonymous reviewers for their constructive comments on the original manuscript. The data presented in this work are archived in the Open Scholarship repository service provided by the Washington University in St. Louis libraries (DOI 10.7936/vy21-vj27).

References

Abers, G., Laura, M., Rondenay, S., Zhang, Z., Wech, A., & Creager, K. (2009). Imaging the source region of Cascadia tremor and intermediate-depth earthquakes. *Geology*, *37*, 1119–1122. https://doi.org/10.1130/G30143A.1

Abers, G. A., Van Keken, P. E., & Hacker, B. R. (2017). The cold and relatively dry nature of mantle forearcs in subduction zones. *Nature Geoscience*, *10*(5), 333–337. https://doi.org/10.1038/ngeo2922

Abramson, E. H., Brown, J. M., Slutsky, L. J., & Zaug, J. (1997). The elastic constants of San Carlos olivine to 17 GPa. *Journal of Geophysical Research*, *102*, 12,253–12,263. https://doi.org/10.1029/97JB00682

Abt, D. L., Fischer, K. M., Abers, G. A., Strauch, W., Protti, J. M., & González, V. (2009). Shear wave anisotropy beneath Nicaragua and Costa Rica: Implications for flow in the mantle wedge. *Geochemistry, Geophysics, Geosystems*, *10*, Q05S15. https://doi.org/10.1029/2009GC002375

Amiguet, E., Moortèle, B., Cordier, P., Hilairet, N., & Reynard, B. (2014). Deformation mechanisms and rheology of serpentines in experiments and in nature. *Journal of Geophysical Research: Solid Earth*, *119*, 4640–4655. https://doi.org/10.1002/2013JB010791

Auzende, A.-L., Escartin, J., Walte, N., Guillot, S., Hirth, G., & Frost, D. (2015). Deformation mechanisms of antigorite serpentinite at subduction zone conditions determined from experimentally and naturally deformed rocks. *Earth and Planetary Science Letters*, *411*, 229–240. https://doi.org/10.1016/j.epsl.2014.11.053

Bachmann, F., Hielscher, R., Jupp, P. E., Pantleon, W., Schaeben, H., & Wegert, E. (2010). Inferential statistics of electron backscatter diffraction data from within individual crystalline grains. *Journal of Applied Crystallography*, *43*, 1338–1355. https://doi.org/10.1107/S0021889810030270X

Bachmann, F., Hielscher, R., & Schaeben, H. (2011). Grain detection from 2D and 3D EBSD data–Specification of the MTEX algorithm. *Ultramicroscopy*, *111*(12), 1720–1733. https://doi.org/10.1016/j.ultramic.2011.08.002

Becker, T. W., Conrad, C. P., Schaeffer, A. J., & Lebedev, S. (2014). Origin of azimuthal seismic anisotropy in oceanic plates and mantle. *Earth and Planetary Science Letters*, *401*, 236–250. https://doi.org/10.1016/j.epsl.2014.06.014

Bezacier, L., Reynard, B., Bass, J., Carmen, S.-V., & Moortèle, B. (2010). Elasticity of antigorite, seismic detection of serpentinites, and anisotropy in subduction zones. *Earth and Planetary Science Letters*, *289*, 198–208. https://doi.org/10.1016/j.epsl.2009.11.009

Bezacier, L., Reynard, B., Cardon, H., Montagnac, G., & Bass, J. (2013). High-pressure elasticity of serpentine and seismic properties of the hydrated mantle wedge. *Journal of Geophysical Research: Solid Earth*, *118*, 527–535. https://doi.org/10.1002/jgrb.50076

Bonatti, E., Emiliani, C., Ferrara, G., Honnorez, J., & Rydell, H. (1974). Ultramafic-carbonate breccias from the equatorial Mid Atlantic Ridge. *Marine Geology*, *16*, 83–102. https://doi.org/10.1016/0025-3227(74)90057-7

Boudier, F., Baronnet, A., & Mainprice, D. (2010). Serpentine mineral replacements of natural olivine and their seismic implications: Oceanic Lizardite versus Subduction-related antigorite. *Journal of Petroleum*, *51*, 495–512. https://doi.org/10.1093/petrology/egp049

Bouilhol, P., Burg, J. P., Bodinier, J. L., Schmidt, M. W., Bernasconi, S. M., & Dawood, H. (2012). Gem olivine and calcite mineralization precipitated from subduction-derived fluids in the kohistan arc-mantle (Pakistan). *The Canadian Mineralogist*, *50*, 1291–1304. https://doi.org/10.3749/canmin.50.5.1291

Bouilhol, P., Burg, J. P., Bodinier, J. L., Schmidt, M. W., Dawood, H., & Hussain, S. (2009). Magma and fluid percolation in arc to forearc mantle: Evidence from Sapat (Kohistan, Northern Pakistan). *Lithos*, *107*, 17–37. https://doi.org/10.1016/j.lithos.2008.07.004

Bouilhol, P., Schaltegger, U., Chiaradia, M., Ovtcharova, M., Stracke, A., Burg, J. P., & Dawood, H. (2011). Timing of juvenile arc crust formation and evolution in the Sapat Complex (Kohistan-Pakistan). *Chemical Geology*, *280*, 243–256. https://doi.org/10.1016/j.chemgeo.2010.11.013

Brownlee, S., Hacker, B., Harlow, G., & Seward, G. (2013). Seismic signatures of a hydrated mantle wedge from antigorite crystal-preferred orientation (CPO). *Earth and Planetary Science Letters*, *375*, 395–407. https://doi.org/10.1016/j.epsl.2013.06.003

Burg, J. (2011). The Asia–Kohistan–India Collision: Review and discussion. In D. Brown, & P. D. Ryan (Eds.), (pp. 279–309). Arc-Continent Collision: Springer. https://doi.org/10.1007/978-3-540-88558-0

Cai, C., Wiens, D., Shen, W., & Eimer, M. (2018). Water input into the Mariana subduction zone estimated from ocean-bottom seismic data. *Nature*, *563*(7731), 389–392. https://doi.org/10.1038/s41586-018-0655-4

Cannat, M., Bideau, D., & Bougault, H. (1992). Serpentinized peridotites and gabbros in the mMid-Atlantic Ridge axial valley at 15°37′N and 16°52′N. *Earth and Planetary Science Letters*, *109*, 87–106.

Capitani, G., & Mellini, M. (2004). The modulated crystal structure of antigorite: The m = 17 polysome. *American Mineralogist*, *89*, 147–158. https://doi.org/10.2138/am-2004-0117

Chernak, L., & Hirth, G. (2010). Deformation of antigorite serpentinite at high temperature and pressure. *Earth and Planetary Science Letters*, *296*, 23–33. https://doi.org/10.1016/j.epsl.2010.04.035

Christensen, N. I. (2004). Serpentinites, peridotites, and seismology. *International Geology Review*, *46*, 795–816. https://doi.org/10.2747/0020-6814.46.9.795

Debret, B., Bouilhol, P., Pons, M. L., & Williams, H. (2018). Carbonate transfer during the onset of slab devolatilization: New insights from fe and Zn stable isotopes. *Journal of Petrology*, *59*, 1145–1166. https://doi.org/10.1093/petrology/egy057

Escartín, J., Hirth, G., & Evans, B. (2001). Strength of slightly serpentinized peridotites: Implications for the tectonics of oceanic lithosphere. *Geology*, *29*, 1023–1026. https://doi.org/10.1130/0091-7613(2001)029<1023:SOSSPI>2.0.CO;2

Evans, B., Johannes, W., Oterbom, H., & Trommsdroff, V. (1976). Stability of chrysotile and antigorite in the serpentine multisystems. *Schweizeriche Mineralogiche*, *56*, 79–93.

Francis, T. J. G. (1981). Serpentinization faults and their role in the tectonics of slow spreading ridges. *Journal of Geophysical Research*, *86*, 616–622.

Fryer, P. (1992). A synthesis of leg 125 drilling of serpentine seamounts on the Mariana and Izu-Bonin forearcs. *Proceeding of the Ocean Drilling Program, Scientific Results*, *125*, 593–614.

Grove, T., Till, C., Lev, E., Chatterjee, N., & Médard, E. (2009). Kinematic variables and water transport control the formation and location of arc volcanoes. *Nature*, *459*(7247), 694–697. https://doi.org/10.1038/nature08044

Guillot, S., Hattori, K., Agard, P., Schwartz, S., & Vidal, O. (2009). Exhumation processes in oceanic and continental subduction contexts: A review. In S. Lallemand, & F. Funiciello (Eds.), *Subduction zone geodynamics*, (pp. 175–205). Berlin Heidelberg: Springer-Verlag. https://doi.org/10.1007/978-3-540-87974-9_10

Guillot, S., Schwartz, S., Reynard, B., Agard, P., & Prigent, C. (2015). Tectonic significance of serpentinites. *Tectonophysics*, *646*, 1–19. https://doi.org/10.1016/j.tecto.2015.01.020

Hacker, B., Peacock, S., Abers, G., & Holloway, S. (2003). Subduction factory 2. Are intermediate-depth earthquakes in subducting slabs linked to metamorphic dehydration reactions? *Journal of Geophysical Research*, *108*(B3), 2030. https://doi.org/10.1029/2001JB001129

Hall, C. E., Fischer, K. M., Parmentier, E. M., & Blackman, D. K. (2000). The influence of plate motions on three-dimensional back arc mantle flow and shear wave splitting. *Journal of Geophysical Research*, *105*, 28,009–28,033. https://doi.org/10.1029/2000jb900297

Hielscher, R., & Schaeben, H. (2008). A novel pole figure inversion method: Specification of the MTEX algorithm. *Journal of Applied Crystallography*, *41*, 1024–1037. https://doi.org/10.1107/S0021889808030112

Hilairet, N., Daniel, I., & Reynard, B. (2006). Equation of state of antigorite, stability field of serpentines, and seismicity in subduction zones. *Geophysical Research Letters*, *33*, L02302. https://doi.org/10.1029/2005GL024728

Hirauchi, K., Katayama, I., Uehara, S., Miyahara, M., & Takai, Y. (2010). Inhibition of subduction thrust earthquakes by low-temperature plastic flow in serpentine. *Earth and Planetary Science Letters*, *295*, 349–357. https://doi.org/10.1016/j.epsl.2010.04.007

Horen, H., Zamora, M., & Dubuisson, G. (1996). Seismic waves velocities and anisotropy in serpentinized peridotites from xigaze ophiolite: Abundance of serpentine in slow spreading ridge. *Geophysical Research Letters*, *23*, 9–12. https://doi.org/10.1029/95GL03594

Huang, Z., Zhao, D., & Wang, L. (2011). Shear wave anisotropy in the crust, mantle wedge, and subducting Pacific slab under northeast Japan. *Geochemistry, Geophysics, Geosystems*, *12*, Q01002. https://doi.org/10.1029/2010GC003343

Hyndman, R., Yamano, M., & Oleskevich, D. (1997). The seismogenic zone of subduction thrust faults. *Island Arc*, *6*, 244–260.

Inoue, S., & Kogure, T. (2012). Electron backscatter diffraction (EBSD) analyses of phyllosilicates in petrographic thin sections. *American Mineralogist*, *97*, 755–758. https://doi.org/10.2138/am.2012.4061

Jan, M. Q., Khan, M. A., & Qazi, M. S. (1993). The Sapat mafic-ultramafic complex, Kohistan arc, North Pakistan. *Geological Society - Special Publications*, *74*, 113–121. https://doi.org/10.1144/GSL.SP.1993.074.01.09

Jung, H. (2011). Seismic anisotropy produced by serpentine in mantle wedge. *Earth and Planetary Science Letters*, *307*, 535–543. https://doi.org/10.1016/j.epsl.2011.05.041

Jung, H. (2018). Crystal preferred orientations of olivine, orthopyroxene, serpentine, chlorite, and amphibole, and implications for seismic anisotropy in subduction zones: A review. *Geosciences Journal*, *21*(6), 985–1011. https://doi.org/10.1007/s12303-017-0045-1

Jung, H., Green, H. W. II, & Dobrzhinetskaya, L. (2004). Intermediate-depth earthquake faulting by dehydration embrittlement with negative volume change. *Nature*, *428*. https://doi.org/10.1038/nature02412

Jung, H., Katayama, I., Jiang, Z., Hiraga, T., & Karato, S. (2006). Effect of water and stress on the lattice-preferred orientation of olivine. *Tectonophysics*, *421*, 1–22. https://doi.org/10.1016/j.tecto.2006.02.011

Juteau, T., Cannat, M., & Lagabrielle, Y. (1990). Serpentinized peridotites in the upper oceanic crust away from transform zones: A comparison of the results of previous DSDP and ODP legs. Proc. Ocean Drill. Program. *Science Results*, *106*(109), 303–308.

Kaproth, B. M., & Marone, C. (2013). Slow earthquakes, preseismic velocity changes, and the origin of slow frictional stick-slip. *Science*, *341*, 1229–1232. https://doi.org/10.1126/science.1239577

Karato, S., Jung, H., Katayama, I., & Skemer, P. (2008). Geodynamic significance of seismic anisotropy of the upper mantle: New insights from laboratory studies. *Annual Review of Earth and Planetary Sciences*, *36*, 59–95. https://doi.org/10.1146/annurev.earth.36.031207.124120

Katayama, I., Hirauchi, K., Michibayashi, K., & Ando, J. (2009). Trench-parallel anisotropy produced by serpentine deformation in the hydrated mantle wedge. *Nature*, *461*(7267), 1114–1117. https://doi.org/10.1038/nature08513

Kneller, E. A., Long, M. D., & van Keken, P. E. (2008). Olivine fabric transitions and shear wave anisotropy in the Ryukyu subduction system. *Earth and Planetary Science Letters*, *268*, 268–282. https://doi.org/10.1016/j.epsl.2008.01.004

Lefeldt, M., Ranero, C., & Grevemeyer, I. (2012). Seismic evidence of tectonic control on the depth of water influx into incoming oceanic plates at subduction trenches. *Geochemistry, Geophysics, Geosystems*, *13*, Q05013. https://doi.org/10.1029/2012GC004043

Léon Soto, G., Ni, J. F., Grand, S. P., Sandvol, E., Valenzuela, R. W., Speziale, M. G., et al. (2009). Mantle flow in the Rivera-Cocos subduction zone. *Geophysical Journal International*, *179*, 1004–1012. https://doi.org/10.1111/j.1365-246X.2009.04352.x

Long, M. D., & Wirth, E. A. (2013). Mantle flow in subduction systems: The mantle wedge flow field and implications for wedge processes. *Journal of Geophysical Research: Solid Earth*, *118*, 583–606. https://doi.org/10.1002/jgrb.50063

Magni, V., Bouilhol, P., & van Hunen, J. (2014). Deep water recycling through time. *Geochemistry, Geophysics, Geosystems*, *15*, 4203–4216. https://doi.org/10.1002/2014GC005525.Received

Mainprice, D., Bachmann, F., Hielscher, R., & Schaeben, H. (2015). Descriptive tools for the analysis of texture projects with large datasets using MTEX: Strength, symmetry and components. *Geological Society, London, Special Publications*, *409*, 251–271. https://doi.org/10.1144/SP409.8

Mainprice, D., Barruol, G., & Ben Ismaïl, W. (2000). The seismic anisotropy of the Earth's mantle: From single crystal to polycrystal. *Geophysical monograph-American Geophysical Union*, *117*, 237–264. https://doi.org/10.1029/GM117p0237

Mainprice, D., Hielscher, R., & Schaeben, H. (2011). Calculating anisotropic physical properties from texture data using the MTEX open-source package. In D. J. Prior, E. H. Rutter, & D. J. Tatham (Eds.), *Deformation mechanisms, rheology and tectonics: Microstructures, mechanics and anisotropy* (pp. 175–192). London, UK: The Geological Society of London. https://doi.org/10.1111/j.1536-7150.1978.tb02790.x

Marquardt, H., Speziale, S., Koch-Müller, M., Marquardt, K., & Capitani, G. C. (2015). Structural insights and elasticity of single-crystal antigorite from high-pressure Raman and Brillouin spectroscopy measured in the (010) plane. *American Mineralogist*, *100*, 1932–1939. https://doi.org/10.2138/am-2015-5198

Mehl, L., Hacker, B., Hirth, G., & Kelemen, P. B. (2003). Arc-parallel flow within the mantle wedge: Evidence from the accreted Talkeetna arc, south central Alaska. *Journal of Geophysical Research*, *108*(B8), 2375. https://doi.org/10.1029/2002JB002233

Mellini, M., Trommsdorff, V., & Compagnoni, R. (1987). Antigorite polysomatism: Behaviour during progressive metamorphism. *Contributions to Mineralogy and Petrology*, *97*, 147–155. https://doi.org/10.1007/BF00371235

Mével, C. (2003). Serpentinization of abyssal peridotites at mid-ocean ridges. *Comptes Rendus Geoscience*, *335*, 825–852.

Morales, L., Mainprice, D., & Boudier, F. (2013). The influence of hydrous phases on the microstructure and seismic properties of a hydrated mantle rock. *Tectonophysics*, *594*, 103–117. https://doi.org/10.1016/j.tecto.2013.03.022

Morales, L. F. G., Mainprice, D., & Kern, H. (2018). Olivine-antigorite orientation relationships: Microstructures, phase boundary misorientations and the effect of cracks in the seismic properties of serpentinites. *Tectonophysics*, *724–725*, 93–115. https://doi.org/10.1016/j.tecto.2017.12.009

Morley, A. M., Stuart, G. W., Kendall, J. M., & Reyners, M. (2006). Mantle wedge anisotropy in the Hikurangi subduction zone, central North Island, New Zealand. *Geophysical Research Letters*, *33*, L05301. https://doi.org/10.1029/2005GL024569

Nakajima, J., Shimizu, J., Hori, S., & Hasegawa, A. (2006). Shear-wave splitting beneath the southwestern Kurile arc and northeastern Japan arc: A new insight into mantle return flow. *Geophysical Research Letters*, *33*, L05305. https://doi.org/10.1029/2005GL025053

Nishii, A., Wallis, S. R., Mizukami, T., & Michibayashi, K. (2011). Subduction related antigorite CPO patterns from forearc mantle in the Sanbagawa belt, southwest Japan. *Journal of Structural Geology*, *33*, 1436–1445. https://doi.org/10.1016/j.jsg.2011.08.006

Padrón-Navarta, J. A., Tommasi, A., Garrido, C. J., & Vicente, S.-V. (2012). Plastic deformation and development of antigorite crystal preferred orientation in high-pressure serpentinites. *Earth and Planetary Science Letters*, *349*, 75–86. https://doi.org/10.1016/j.epsl.2012.06.049

Peacock, S. M., & Hyndman, R. D. (1999). Hydrous minerals in the mantle wedge and the maximum depth of subduction thrust earthquakes. *Geophysical Research Letters*, *26*, 2517–2520.

Piñero-Feliciangeli, L. T., & Kendall, J. M. (2008). Sub-slab mantle flow parallel to the Caribbean plate boundaries: Inferences from SKS splitting. *Tectonophysics*, *462*, 22–34. https://doi.org/10.1016/j.tecto.2008.01.022

Pozgay, S. H., Wiens, D. A., Conder, J. A., Shiobara, H., & Sugioka, H. (2007). Complex mantle flow in the Mariana subduction system: Evidence from shear wave splitting. *Geophysical Journal International*, *170*, 371–386. https://doi.org/10.1111/j.1365-246X.2007.03433.x

Ranero, C., Morgan, J. P., McIntosh, K., & Reichert, C. (2003). Bending-related faulting and mantle serpentinization at the Middle America trench. *Nature*, *425*(6956), 367–373. https://doi.org/10.1038/nature01961

Reynard, B. (2013). Serpentine in active subduction zones. *Lithos*, *178*, 171–185. https://doi.org/10.1016/j.lithos.2012.10.012

Rüpke, L., Morgan, J., Hort, M., & Connolly, J. (2004). Serpentine and the subduction zone water cycle. *Earth and Planetary Science Letters*, *223*, 17–34. https://doi.org/10.1016/j.epsl.2004.04.018

Savage, M. K. (1999). Seismic anisotropy and mantle deformation: What have we learned from shear wave splitting? *Reviews of Geophysics*, *37*, 65–106.

Schmidt, M., & Poli, S. (1998). Experimentally based water budgets for dehydrating slabs and consequences for arc magma generation. *Earth and Planetary Science Letters*, *163*, 361–379. https://doi.org/10.1016/S0012-821X(98)00142-3

Skemer, P., & Hansen, L. N. (2016). Inferring upper-mantle flow from seismic anisotropy: An experimental perspective. *Tectonophysics*, *668–669*, 1–14. https://doi.org/10.1016/j.tecto.2015.12.003

Skemer, P., Warren, J. M., & Hirth, G. (2012). The influence of deformation history on the interpretation of seismic anisotropy. *Geochemistry, Geophysics, Geosystems*, *13*, Q03006. https://doi.org/10.1029/2011gc003988

Smith, G. P., Wiens, D. A., Fischer, K. M., Dorman, L. M., Webb, S. C., & Hildebrand, J. A. (2001). A complex pattern of mantle flow in the Lau backarc. *Science*, *292*, 713–716. https://doi.org/10.1126/science.1058763

Syracuse, E. M., van Keken, P. E., Abers, G. A., Suetsugu, D., Bina, C., Inoue, T., et al. (2010). The global range of subduction zone thermal models. *Physics of the Earth and Planetary Interiors*, *183*, 73–90. https://doi.org/10.1016/j.pepi.2010.02.004

Ulmer, P., & Trommsdorff, V. (1995). Serpentine stability to mantle depths and subduction-related magmatism. *Science*, *268*, 858–861. https://doi.org/10.1126/science.268.5212.858

Van De Moortèle, B., Bezacier, L., Trullenque, G., & Reynard, B. (2010). Electron back-scattering diffraction (EBSD) measurements of antigorite lattice-preferred orientations (LPO). *Journal of Microscopy*, *239*, 245–248. https://doi.org/10.1111/j.1365-2818.2010.03398.x

Viti, C., & Mellini, M. (1998). Mesh textures and bastites in the Elba retrograde serpentinites. *European Journal of Mineralogy*, *10*(6), 1341–1360. https://doi.org/10.1127/ejm/10/6/1341

White, R. S., Detrick, R., Sinha, M. C., & Cormier, M. H. (1984). Anomalous seismic crustal structure of oceanic fracture zones. *Geophysical Journal of the Royal Astronomical Society*, *79*, 779–798.

Wunder, B., & Schreyer, W. (1997). Antigorite: High-pressure stability in the system MgO-SiO2-H2O (MSH). *Lithos*, *41*, 213–227.